Title

Point defect model for passivity breakdown on hyper-duplex stainless steel 2707 in solutions containing bromide at different temperatures

Permalink

https://escholarship.org/uc/item/9v30z379

Authors

Sun, Li
Zhao, Tianyu
Qiu, Jie
et al.

Publication Date

2022

DOI

10.1016/j.corsci.2021.109959

Peer reviewed

Point defect model for passivity breakdown on hyper-duplex stainless steel 2707 in solutions containing bromide at different temperatures

Li Sun [a,b,c], Tianyu Zhao [b], Jie Qiu [b], Yangting Sun [c,*], Kuijiao Li [a], Haibing Zheng [a], Yiming Jiang [c], Yanhui Li [d], Jin Li [c], Weihua Li [a], Digby D. Macdonald [b,*]

[a] School of Chemical Engineering and Technology, Sun Yat-sen University, Zhuhai 519082, China
[b] Department of Nuclear Engineering, University of California at Berkeley, Berkeley, CA 94720, United States
[c] Department of Materials Science, Fudan University, Shanghai 200433, China
[d] Key Laboratory of Thermo-Fluid Science and Engineering of MOE, School of Energy and Power Engineering of Xi'an Jiaotong University, Xi'an, Shaanxi 710049, China

A B S T R A C T

Passivity breakdown on HDSS 2707 has been studied and the electrochemical data are interpreted in terms of the Point Defect Model. Pitting parameters of HDSS 2707 are determined, including the polarizability at bl/s interface, the defect annihilation rate, and the defect diffusion coefficient. The breakdown potential is demonstrated to be linearly related to log [Br⁻], pH, and the square root of potential scan rate ($v^{1/2}$), and follows a near-normal distribution. The critical vacancy concentration calculated from the PDM is consistent with that estimated crystallographically from the chromic barrier layer, and the dominant point defect is further confirmed by Mott-Schottky measurements.

1. Introduction

Hyper-duplex stainless steel 2707 (HDSS 2707) was developed to serve in extreme corrosive environments, such as heat exchanger system, refining equipment, and acid water/gas separation towers, because of its pitting resistance equivalent number (PREN = wt% Cr + 3.3 wt% Mo + 16 wt% N]) is more than 48, compared to that of DSS 2205 which is about 34 [1–6]. Previous investigations showed that the potentiostatic critical pitting temperature (CPT) of HDSS 2707 in 1 M and even in 3 M NaCl solution is above 100 ℃, indicating that the breakdown potential (E_b) cannot be obtained by the potentiodynamic polarization technique in NaCl solution when the temperature is below 100 ℃ at atmospheric pressure [3]. However, a higher pitting resistance is a relative concept, the corrosion failure of HDSS 2707 occurs when bromide anions are present, and we obtained the CPT in 1 M NaBr solution at about 68 ℃ at atmospheric pressure [3]. Accordingly, the passive film formed on HDSS 2707 is not completely resistant to passivity breakdown, and metastable pits grow to critical dimension, thereby acting as the sites for the nucleation of stress corrosion cracking (SCC) [7]. Previous researchers focused on the effects of alloying elements, e.g., Si, Ce, Cu and W, on the precipitated phases and their relationships to intergranular corrosion (IGC) and pitting resistance of HDSS 2707 [8–11]. Besides, the

relationships between solution heat treatment and the resulting sensitization, as well as the impact of welding, both resulting in microstructure evolution, and the phase precipitation and the IGC of HDSS 2707 have been comprehensively analyzed [12–15]. Nevertheless, pitting occurs and the mechanisms of passivity breakdown and pitting on HDSS 2707 has not been explained in detail, and the pitting parameters for HDSS 2707 are not reported in previous papers.

The point defect model (PDM) has been successfully employed to describe the growth and breakdown of passive films on alloys and metals (including HDSS 2707), providing a theoretical basis for explaining pitting in aggressive environments [16–21]. The PDM postulates that the barrier layer of a bi-layer passive film comprising a point defective barrier layer (bl) and a non-defective, precipitated outer layer (ol) can be described in terms of a set of defect generation/annihilation reactions that occur at the metal/barrier layer (m/bl) and barrier layer/solution (bl/s) interfaces as depicted in Fig. 1.

In describing passivity breakdown, aggressive (breakdown-inducing) anions (e.g., Cl⁻, Br⁻, F⁻) absorb into a surface oxygen vacancy (Eq. 1); then the system compensates for the loss of oxygen vacancies by generating cation vacancy/oxygen vacancy pairs via a Schottky-pair type of reaction (Eq. 2) [22] or by the ejection of a cation from the surface of the barrier layer (bl). The oxygen vacancies in turn react with

* Corresponding authors.
E-mail addresses: sunyangting@fudan.edu.cn (Y. Sun), macdonald@berkeley.edu (D.D. Macdonald).

Metal | **Barrier Layer ($MO_{\chi/2}$)** | **Precipitated Layer**

(R1) $m + V_M^{\chi'} \xrightarrow{k_1} M_M + V_m + \chi e'$

(R2) $m \xrightarrow{k_2} M_i^{\chi+} + V_m + \chi e'$

(R3) $m \xrightarrow{k_3} M_M + \left(\frac{\chi}{2}\right)V_{\ddot{O}} + \chi e'$

(R4) $M_M \xrightarrow{k_4} M^{\delta+}(aq) + V_M^{\chi'} + (\delta - \chi)e'$

(R5) $M_i^{\chi+} \xrightarrow{k_5} M^{\delta+}(aq) + (\delta - \chi)e'$

(R6) $V_{\ddot{O}} + H_2O \xrightarrow{k_6} O_O + 2H^+$

(R7) $MO_{\chi/2} + \chi H^+ \xrightarrow{k_7} M^{\delta+}(aq) + \frac{\chi}{2}H_2O + (\delta - \chi)e^-$
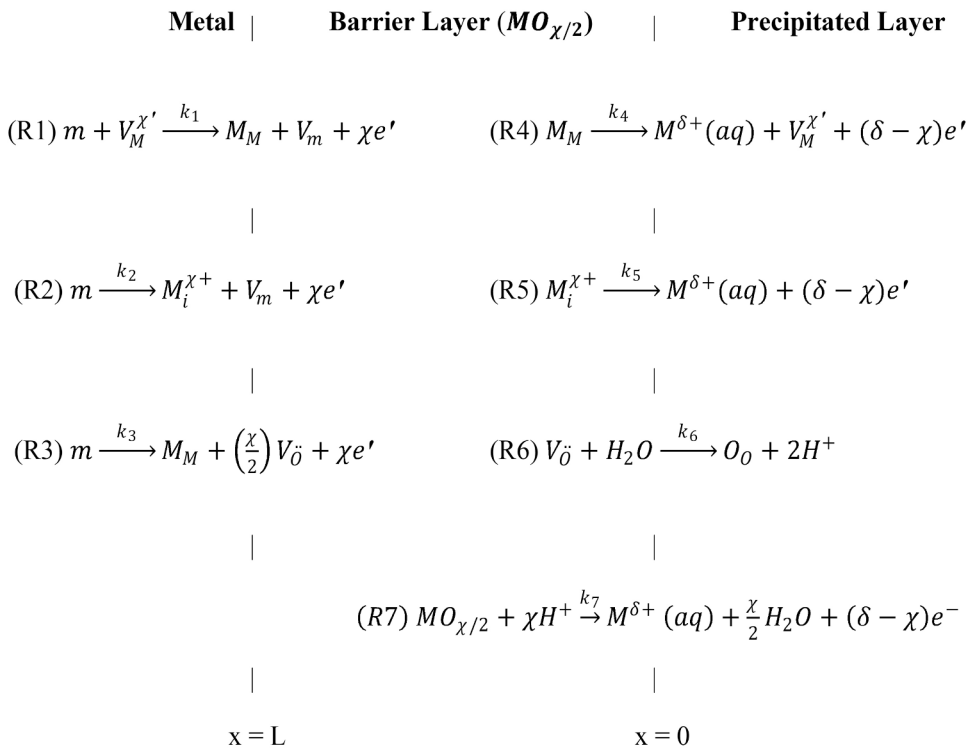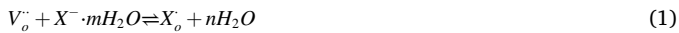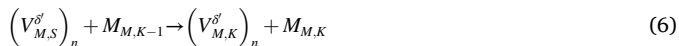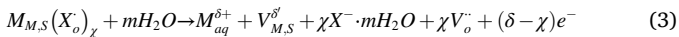
x = L   x = 0

Fig. 1. Summary of the defect generation and annihilation reactions envisioned to occur at the interfaces of the barrier oxide layer on a metal, according to the PDM. $V_M^{\chi'}$ is a cation vacancy, $M_i^{\chi+}$ is a cation interstitial, $V_{\ddot{O}}$ is an oxygen (anion) vacancy, $M^{\delta+}(aq)$ is a cation in outer layer/solution interface, M_M is a cation in cation site on the cation sublattice, O_O is an oxide ion in anion site on the anion sublattice, $MO_{\chi/2}$ is the stoichiometric barrier layer oxide. Note that the origin of the coordinate system is the bl/s interface and hence that the flux of oxygen vacancies is negative.

additional anions (e.g., Br⁻ in this paper) at the barrier layer/solution interface to generate more cation vacancies in a cyclical process. Thus, the principal cation vacancy generation mechanisms that occur in response to the absorption of X^- into V_o can be depicted as:

$$V_o^{\cdot\cdot} + X^- \cdot mH_2O \rightleftharpoons X_o^{\cdot} + nH_2O \tag{1}$$

$$Null \xrightarrow{Schottky} \frac{\chi}{2}V_o^{\cdot\cdot} + V_M^{\chi'} \tag{2}$$

or via cation abstraction [23]:

$$M_{M,S}(X_o)_\chi + mH_2O \rightarrow M_{aq}^{\delta+} + V_{M,S}^{\delta'} + \chi X^- \cdot mH_2O + \chi V_o^{\cdot\cdot} + (\delta - \chi)e^- \tag{3}$$

$$V_{M,S}^{\delta'} + M_{M,S-1} \rightarrow V_{M,S-1}^{\delta'} + M_{M,S} \tag{4}$$

$$\bullet$$
$$\bullet$$

$$V_{M,J}^{\delta'} + M_{M,J-1} \rightarrow V_{M,J-1}^{\delta'} + M_{M,J} \tag{5}$$

$$\bullet$$
$$\bullet$$

$$\left(V_{M,S}^{\delta'}\right)_n + M_{M,K-1} \rightarrow \left(V_{M,K}^{\delta'}\right)_n + M_{M,K} \tag{6}$$

where $V_o^{\cdot\cdot}$ is an oxygen vacancy, X^- is the aggressive anions, $M_{M,S}(X_o)_\delta$ is cation vacancy/oxygen vacancy pair in the bl surface, $M_{M,S}$ is a cation in the cation sublattice in the bl surface, $M_{M,S-1}$ is a cation in the cation sublattice on first cation layer below the surface, $V_M^{\chi'}$ is cation vacancies, $V_{M,S}^{\delta'}$ is a cation vacancy in the surface of the barrier layer, and $V_{M,S-1}^{\delta'}$ is a cation vacancy on the cation layer immediately below the bl surface. The reactions occur cyclically, resulting in the transmission of cation vacancies via migration from the bl surface to the m/bl interface where they progressively condense to form the cation vacancy condensate $\left(V_{M,S-1}^{\delta'}\right)_n$. Note that Reactions (1) and (3) – (5) occur for each occurrence of Reaction (6) to form the cumulative vacancy condensate, $\left(V_{M,S-1}^{\delta'}\right)_n$. It is this entity that causes separation of the bl from the metal,

resulting in cessation of the growth of the bl into the substrate metal at the condensation point and, ultimately, in passivity breakdown via dissolution of the bl "cap" over the condensation point that is unmatched by growth of the bl into the metal. Both of the mechanisms outlined above (Schottky pair and cation abstraction) give rise to identical functional forms for the dependencies of the critical breakdown voltage (V_C) and induction time (t_{ind}) on system independent variables, such as chloride activity, pH, potential (t_{ind} only), and temperature, although the model parameters contained in each are frequently unique [21,22].

The migration of cation vacancies across the barrier layer (bl) toward the metal/bl interface is driven by the high electric field (ε) that exists within the bl of the passive film. In the PDM, the electric field strength is postulated to be buffered by Esaki (band-to-band) tunneling and hence is independent of applied voltage [24]. Thus, under steady-state conditions, the electric field strength within the bl is in the expected range of $(1 \sim 5) \times 10^6$ V/cm and deviates from the steady-state value under transient polarization conditions; i.e., it is likely to be sweep rate-dependent, because the defects structure of the bl relaxes only very slowly [25,26]. Finally, the migrating cation vacancies annihilate at the metal/bl interface can be seen in Reaction (R1) in Fig. 1 [25,27]. The annihilation rate is designated J_m and its role in determining V_C and t_{ind} for passivity breakdown is discussed further below. However, the ability of this reaction to annihilate cation vacancies is limited by the rate constant, k_1, which, in the steady-state, is independent of applied potential or is only weakly dependent on potential, depending upon the system. This is, because in the expression for the rate constant:

$$k_1 = k_1^0 e^{a_1 V} e^{b_1 L_{ss}} e^{c_1 pH} \tag{7}$$

the quantity $a_1 V + b_1 L_{ss} =$ const via exact compensation between the effects of the applied voltage, V, and the resulting barrier layer thickness, L_{ss}, on k_1 when no change occurs in the oxidation state of the cation upon ejection from the bl (i.e., $\delta = \chi$). If $\delta \neq \chi$, $a_1 V + b_1 L_{ss}$ is a weak function of V. L_{ss} is the steady-state thickness of the bl [27].

Thus, as the applied voltage increases, the flux rate of cation vacancies across the bl from the bl/s interface where they are formed by Reaction R4 to the m/bl interface where they are annihilated by Reac-
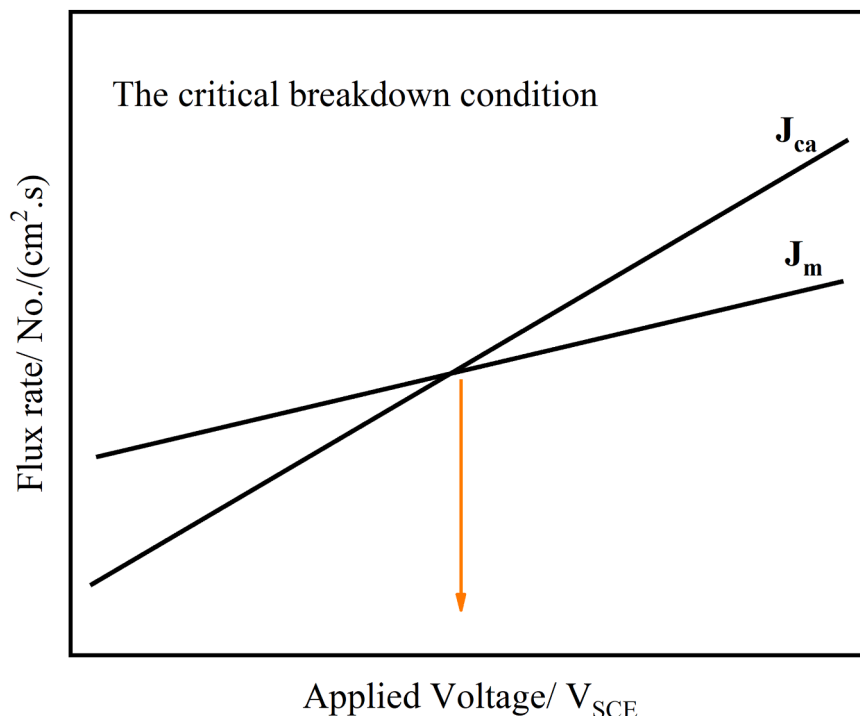
Fig. 2. Schematic of the relative dependencies of J_m and J_{ca} on the applied voltage, V_{SCE}.

tion R1 in Fig. 1 also increases, as given by the Nernst-Planck equation for migration:

$$J_{ca} = \chi\gamma D\varepsilon C_{V_M}^{bl/s} \qquad (8)$$

where $\gamma = F/RT$, D is the cation vacancy diffusivity in the bl, ε is the electric field strength, and $C_{V_M}^{bl/s}$ is the concentration of cation vacancies at the bl/s interface as established by the vacancy generation mechanisms described above. Thus, the changes in the flux rate J_m and J_{ca} as a function of applied voltage are depicted schematically in Fig. 2. This figure displays the relationships between the fluxes J_m and J_{ca} with the critical breakdown voltage corresponding to the condition $J_m = J_{ca}$ [27, 28]. Although k_1 is constant for $\delta = \chi$, it still depends on potential, because $C_{V_M}^{bl/s}$ depends on the applied potential. This is because the rate constant k_4 is an exponential function of V; a dependence that is not compensated for by an increase in L_{ss} (note that $b_4 = 0$, because Reaction R4 occurs at the bl/s interface [25,26].

As noted above, the PDM proposes that the cation vacancies arriving at the m/bl interface are annihilated by the emission of cations from the metal into the vacancies [27]. If the annihilation rate, defined as J_m, is incapable of consuming the cation vacancies arriving at the metal/bl interface, because of an excessively high J_{ca}, the excess vacancies will condense at the m/bl interface, either on the adjacent layer of the cation sublattice as $V_M^{x'}$ or, possibly on the adjacent layer of the metal lattice as V_m.

$$J_m = k_1^0 exp(a_1 V + b_1 Lss + c_1 pH)C_{V_M}^{m/bl} \qquad (9)$$

This process is envisioned to initially begin at a point of atomic dimension subtending a region of the bl that has an abnormally high J_{ca}, most likely due to a high cation vacancy diffusivity but perhaps also due to a high $C_{V_M}^{bl/s}$ (see Eq. 8). In any event, continued cation vacancy condensation is postulated to occur at the periphery of this nucleus, resulting in the continual expansion of the condensate. The condensate results in decohesion of the bl from the substrate metal and hence in cessation of bl growth into the metal via the generation of oxygen vacancies (Reaction R3, Fig. 1). Simultaneously, the bl "cap" over the

nucleus continues to dissolve such that the condensate will achieve a critical size (radius) at the time of cap rupture.

In previous researches, PDM theory has been successfully applied in interpreting the pitting behaviors of austenite stainless steels, ferrite stainless steels, and multiphase alloys such as Al-Li and Al-Zn-Mg, and have obtained the pitting parameters of these metals [29–33]. However, the available information on pitting mechanisms of the duplex stainless steels, especially the hyper-duplex stainless steel is still very rare. In this paper, the PDM is employed to investigate the pitting predictions as a function of temperature, Br⁻ concentration, pH and potential scan rate, and gives the pitting parameters of HDSS 2707.

2. Experimental

HDSS 2707 plate, provided by Sandvik company, was cut into specimens with dimensions of $12 \times 6 \times 2$ mm and has a chemical composition of Cr 26.99 wt%, Ni 6.48 wt%, Mo 4.89 wt%, C 0.017 wt%, N 0.36 wt%, Cu 0.13 wt%, Mn 1.00 wt% and Fe bal, which was determined by chemical analysis at the Shanghai material testing center. The as-received samples were initially subjected to the annealing treatment at 1100 ℃ in an inert nitrogen atmosphere for 30 min to assure a structural homogenization before quenching in water [3]. Prior to each test, the specimens were abraded down to 2000 grit sandpaper, and then cleaned ultrasonically in acetone, alcohol, and deionized water, and was finally dried in hot air. The concentration of NaBr is 0.5 M, 1 M, 2 M, and 3 M. The temperature is controlled at 70 ± 1 ℃, 80 ± 1 ℃ and 90 ± 1 ℃ by using the thermostatic water bath. The pH of NaBr solution is adjusted to 5.1 ± 0.1, 6.0 ± 0.1, 7.1 ± 0.1, and 8.1 ± 0.1 by using acetic acid/sodium hydroxide.

A typical three-electrode system was used to conduct electrochemical experiments by using a potentiostat workstation CHI 660D. The cell contained a platinum foil as the counter electrode, a saturated calemol electrode (SCE) as the reference electrode, and a HDSS 2707 specimen as the working electrode with an exposed area of 0.25 cm². For potentiodynamic polarization measurements, the working electrode was cathodically polarized at -1.2 V_{SCE} for 120 s to remove the air-formed oxidation products and to improve reproducibility. A twenty-minute
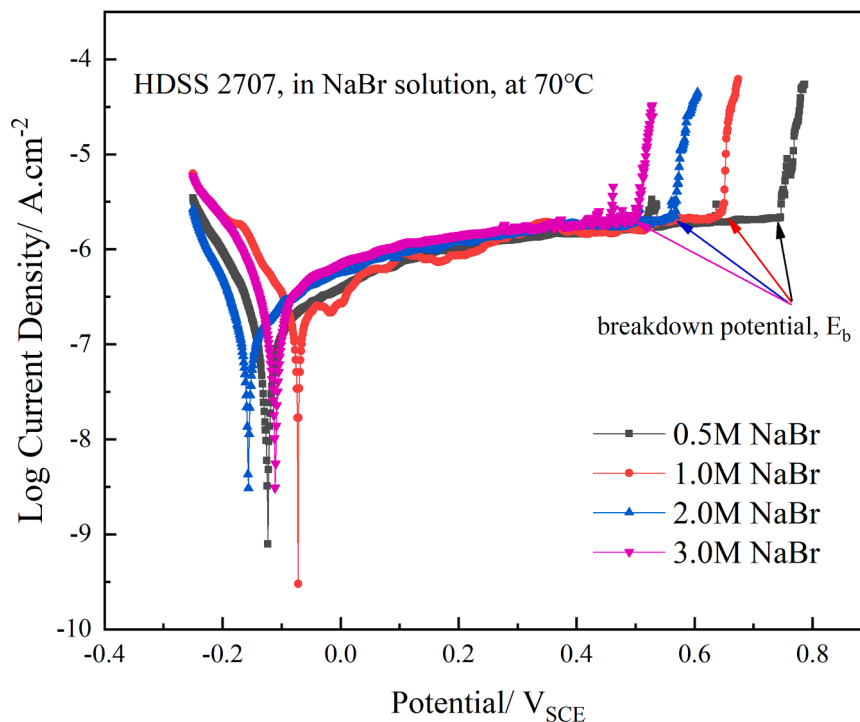
Fig. 3. Typical potentiodynamic polarization curves for HDSS 2707 in NaBr solutions at the scan rate of 1.667 mV/s.
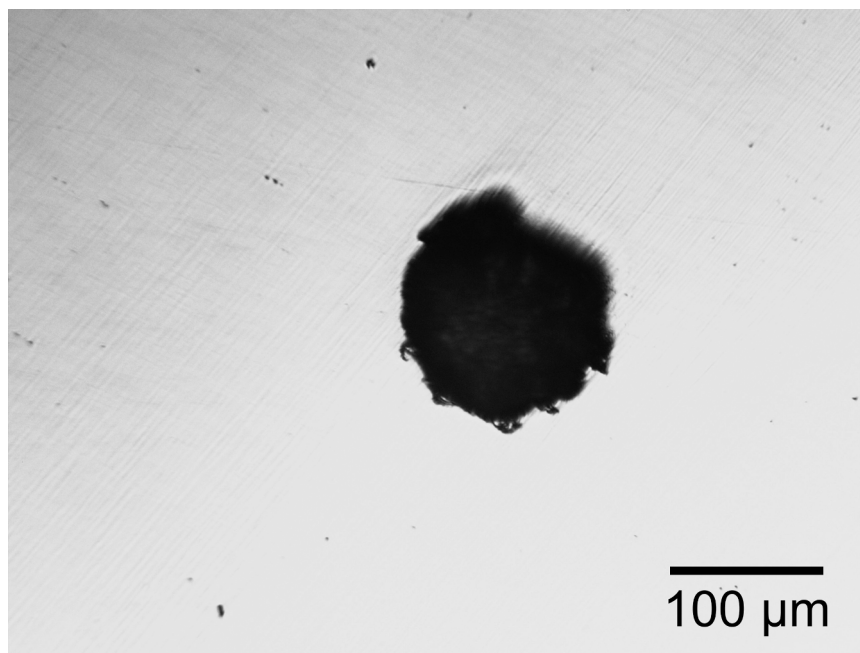

Fig. 4. Typical OM morphology of pitting on HDSS 2707 in NaBr solution after potentiodynamic polarization test.

rest at the open circuit potential (OCP) was then allowed before conducting potentiodynamic polarization, scanned at the scan rate of 1.667 mV/s from −0.25 V_{SCE} (about −0.1 V_{SCE} lower than stable OCP) to the occurrence of a stable pit. The scan on each specimen was repeated 20 times to obtain the cumulative distributions of the breakdown potential (E_b). Pitting corrosion was confirmed by an optical microscopy (OM) after each experiment. In order to study the effects of potential scan rates on E_b, four scan rates, i.e., 0.5 mV/s, 1.667 mV/s, 5.667 mV/s and 10 mV/s were employed.

The Mott-Schottky (M-S) analysis was carried out to study the semiconductor characteristics and the donor densities of the passive film on HDSS 2707 in NaBr solution by measuring the capacitance of the interface as a function of applied potential from − 0.2 V_{SCE} to 0.7 V_{SCE}. This was done dynamically by superimposing a voltage sine wave of 10 mV at 1000 Hz frequency sweeping the potential in the negative direction at a sweep rate of 20 mV/s [34].
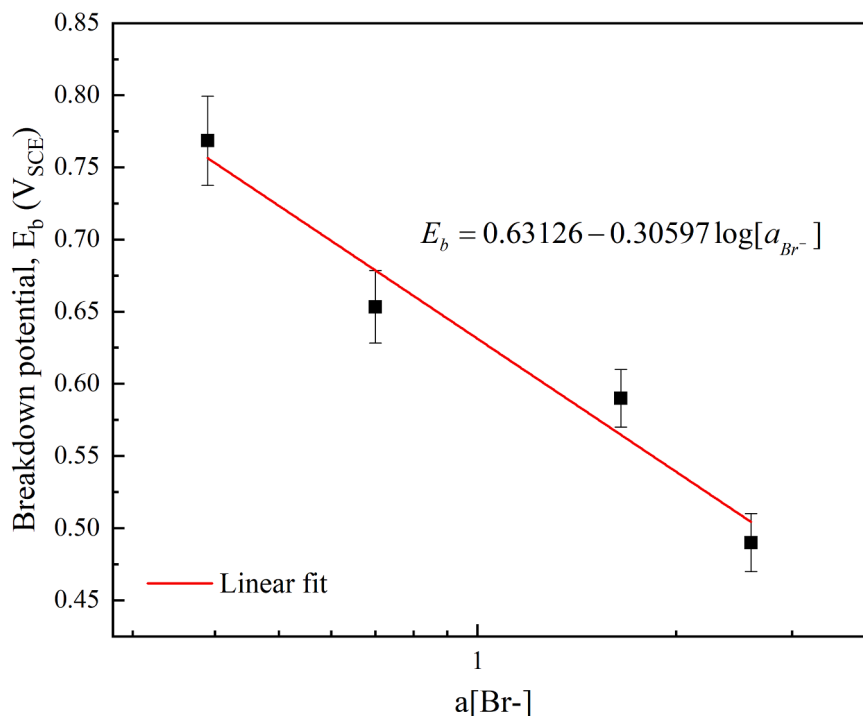
$$E_b = 0.63126 - 0.30597 \log[a_{Br^-}]$$

Fig. 5. The mean in distribution in the breakdown potentials of HDSS 2707 as a function of bromide ions activity at the scan rate of 1.667 mV/s, at 70 ℃.
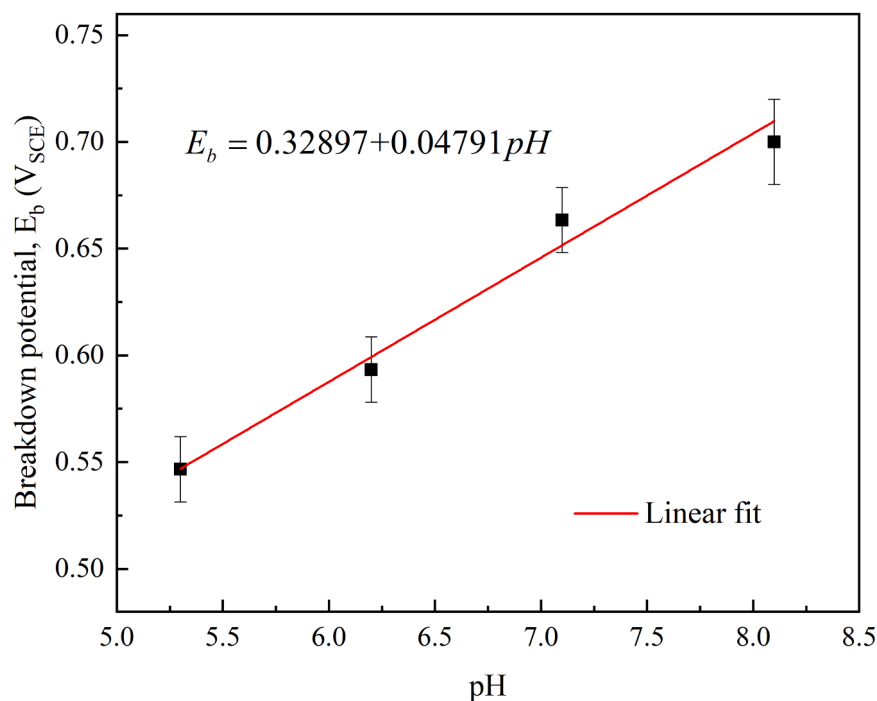

$$E_b = 0.32897 + 0.04791 pH$$

Fig. 6. The mean in distribution in the breakdown potentials as a function of pH in 1 M NaBr at 70 ℃.

3. Results and discussion

3.1. The effect of bromide ions on pitting

Fig. 3 shows the typical potentiodynamic polarization curves of HDSS 2707 in NaBr solution at 70 ℃ (pH = 8.1 ± 0.1) as a function of bromide concentration, at an applied potential sweep rate of v = 1.667 mV/s. The polarization curves display a wide, stable passive region (about 0.1 V$_{SCE}$ ~ 0.5 V$_{SCE}$) with the passive current density at

$\sim 10^{-6} A/cm^{-2}$, terminating in a sharp rise in the current density at a potential that depends on the bromide concentration, due to the sudden occurrence of passivity breakdown. The breakdown potential (E_b) of HDSS 2707 is seen to decrease with increasing bromide concentration. According to the PDM, the aggressive ion (Br$^-$) adsorbs into surface oxygen vacancies and produce cation vacancies at the bl/s interface that then condense at the m/bl interface, as described above. Thus, at higher bromide concentrations, more cation vacancies are produced, and the excess vacancies are envisioned to condense either on the cation
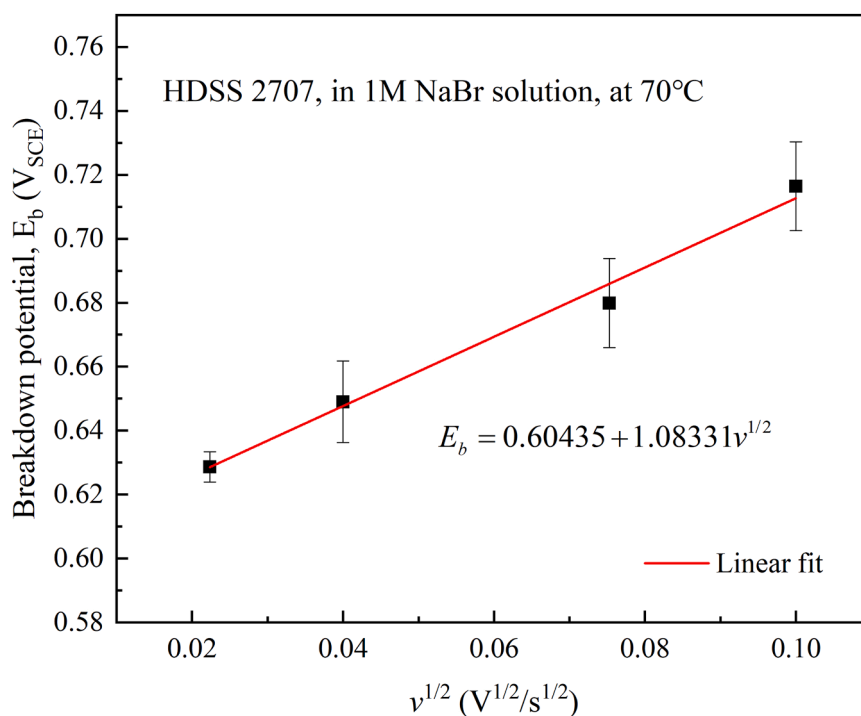
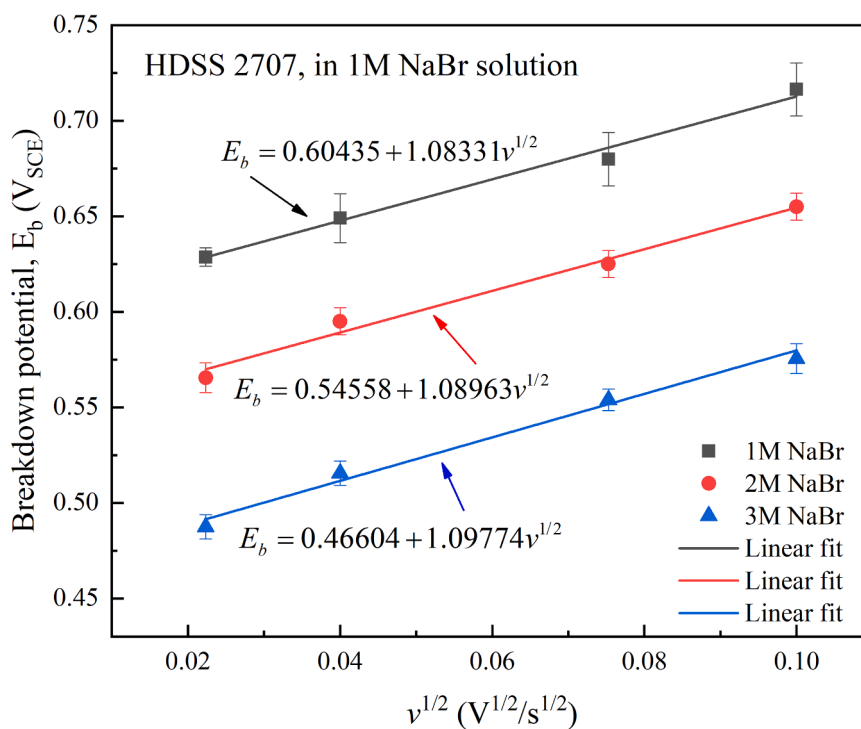Fig. 7. The mean in distribution in the critical breakdown potential as a function of potential scan rate.

Fig. 8. Measured breakdown potential at different potential scan rates for HDSS 2707 with different bromide concentration with measured pH = 8.2 ± 0.1.

sublattice or on the lattice of substrate metal at the m/bl interface, resulting in the separation of the bl from the substrate metal. The passive film eventually ruptures under the dissolution at the bl/s interface, augmented by stress, and passivity breakdown and subsequently pitting occurs [35]. The inflection point at which the current density suddenly increases is defined as the breakdown potential (E_b), and the stable pitting morphology is inspected in Fig. 4.

The PDM expresses the dependence of the E_b (or V_c) on temperature,

pH, and anion activity as given by Eqs. (10) to (12), which show that V_c decreases linearly with increasing $\log(a_x)$ and with decreasing pH, where a_x is the activity of the aggressive anion (e.g., Br⁻), [35].

$$V_c = \frac{4.606RT}{\chi \alpha F} log\left(\frac{b}{D}\right) - \frac{2.303RT}{\alpha F} log(a_{Br^-}) \qquad (10)$$
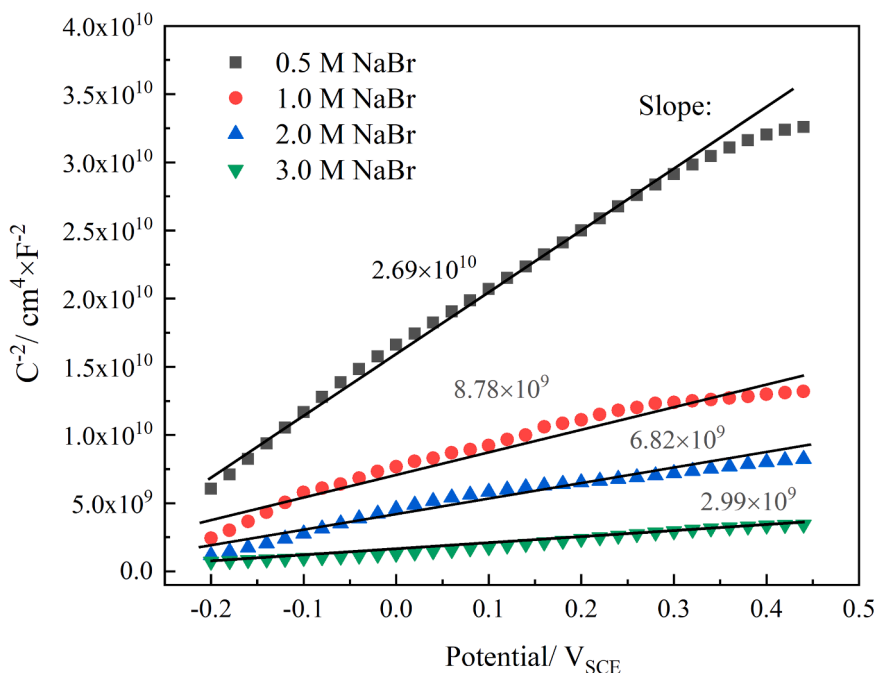
Fig. 9. Mott-Schottky plots of the passive film on HDSS 2707 in NaBr solution at 70 ℃.
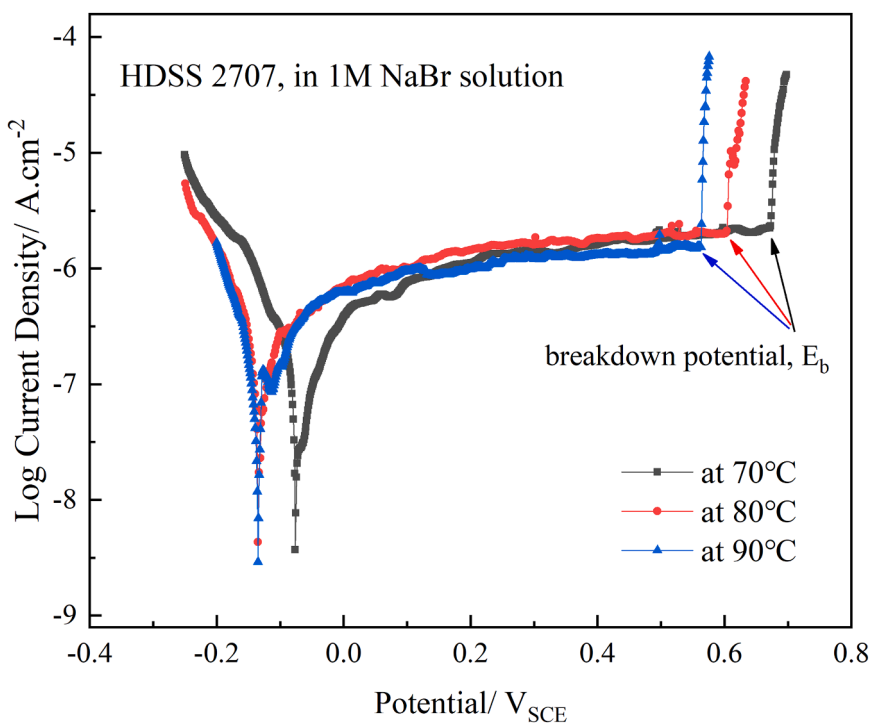

Fig. 10. Typical potentiodynamic polarization curves for HDSS 2707 in 1 M NaBr solutions with different temperatures at the scan rate of 1.667 mV/s.

$$b = \frac{RTJ_m\Omega}{F\chi\varepsilon N_v} \cdot exp\left(\frac{w - \frac{\chi}{2}\beta FpH}{RT}\right)$$

$$= \frac{RTJ_m\Omega}{F\chi\varepsilon N_v} \cdot exp\left(\frac{\Delta G_s^0 + \frac{\chi}{2}\Delta G_A^0 - \frac{\chi}{2}\beta FpH - \frac{\chi}{2}F\phi_{f/s}^0}{RT}\right) \quad (11)$$

$$\phi_{f/s} = \phi_{f/s}^0 + \alpha V + \beta pH \quad (12)$$

where D is the diffusivity of the cation vacancy in the bl, and b is defined in Eq. (11). The parameters χ, ε, and Ω are the oxide stoichiometry

($MO_{\chi/2}$), the electric field strength, and the volume per mole of cation of the passive film, respectively. In Eq. (11), the energy term, w, is defined in Eq. (13) to describe the energy related to the absorption of Br⁻ into [36].

$$w = \Delta G_s^0 + \frac{\chi}{2}\Delta G_A^0 - \frac{\chi}{2}F\phi_{f/s}^0 \quad (13)$$

A negative value of w means the absorption process is energetically-favorable. ΔG_s^0 and G_A^0 are the change in standard Gibbs energy for the Schottky-pair reaction (Eq. 2) and for the absorption of Br⁻ into oxygen
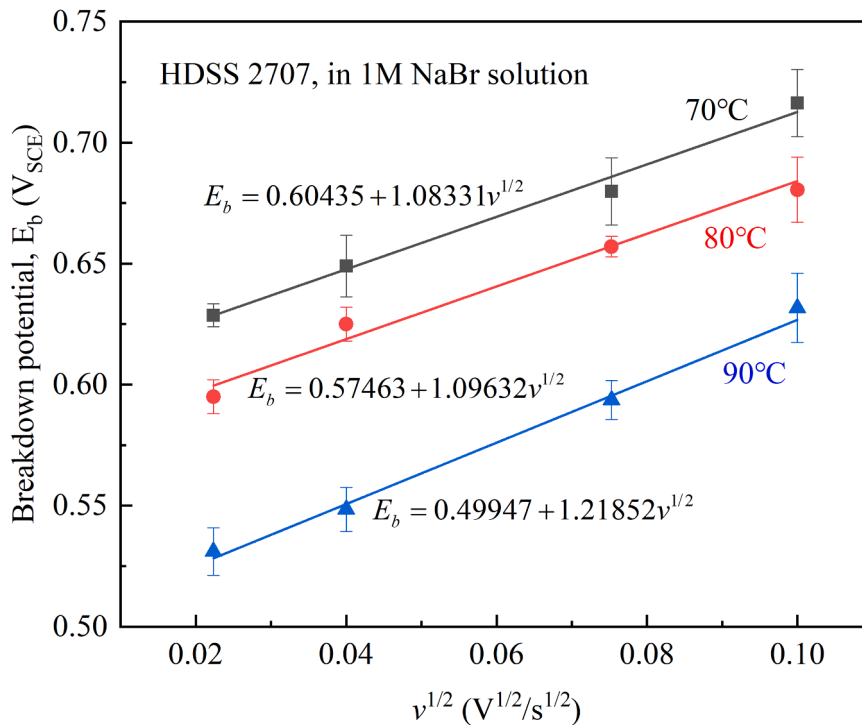
Fig. 11. Measured breakdown potential at different potential scan rates for HDSS 2707 in 1 M NaBr with different temperatures at pH = 8.1 ± 0.1.
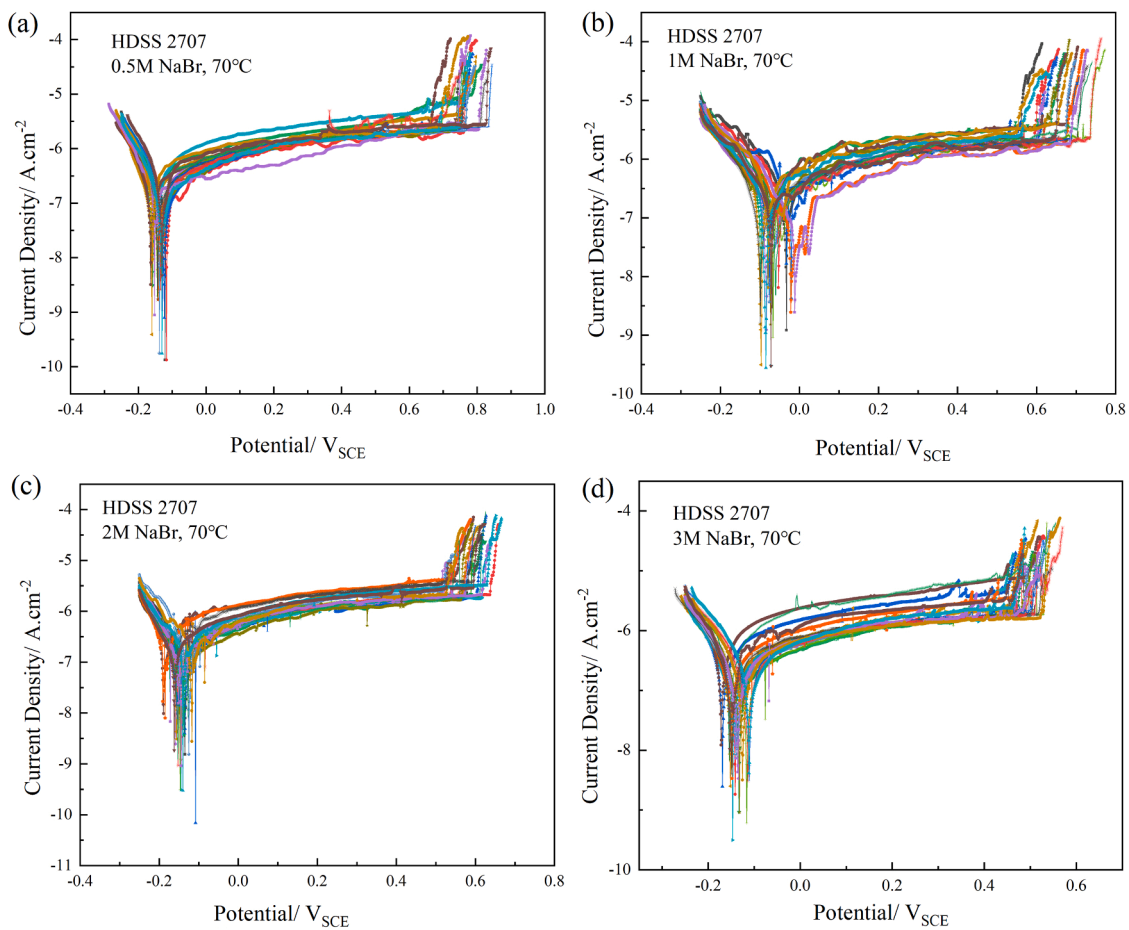

Fig. 12. Replication of potentiodynamic polarization curves for HDSS 2707 in NaBr solutions as a function of bromide concentrations: (a) 0.5 M; (b) 1 M; (c) 2 M; (d) 3 M.
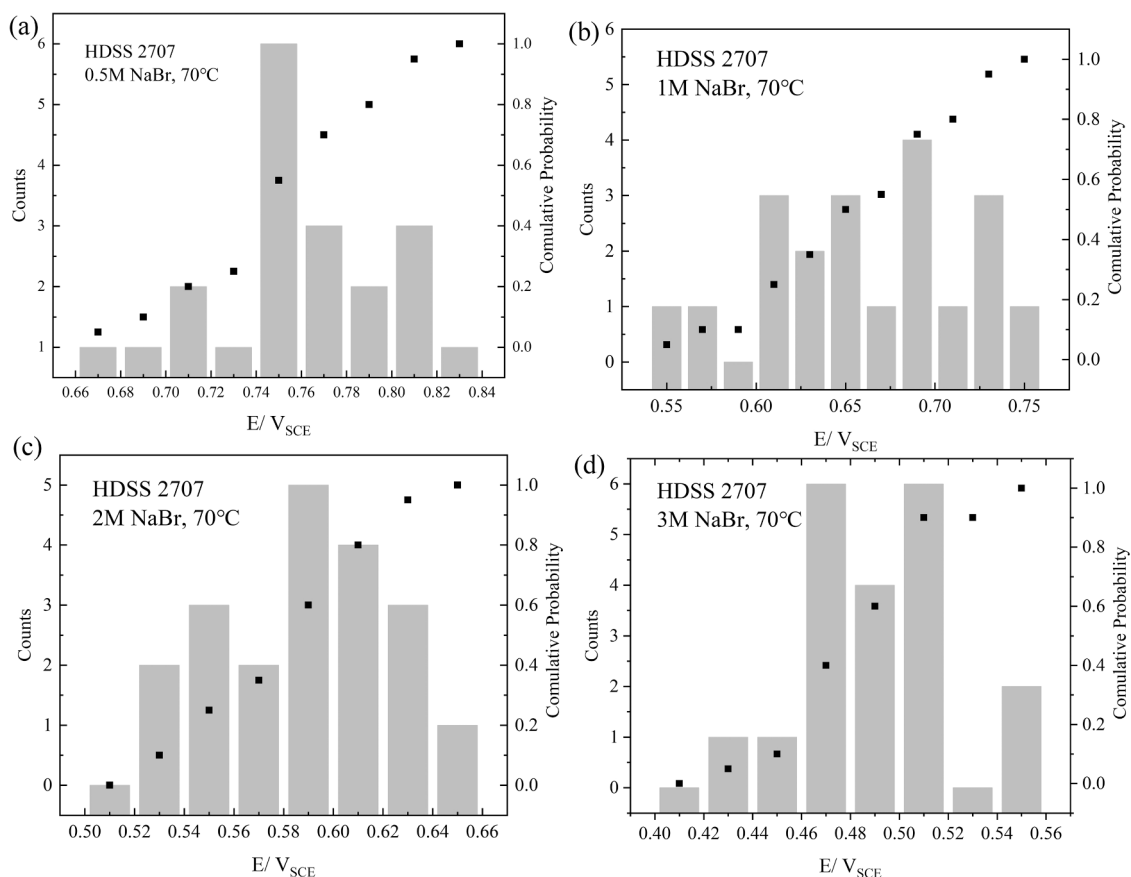
Fig. 13. Cumulative distributions of breakdown potential (V_c/E_b) in solutions as a function of Br⁻ concentrations: (a) 0.5 M; (b) 1 M; (c) 2 M; (d) 3 M.

vacancies at the film/solution surface and α and β are the dependence of the potential drop across the bl/solution interface ($\phi_{f/s}$) on the applied voltage and pH, respectively. The parameter $\phi_{f/s}^0$ is the value of $\phi_{f/s}$ in the standard state of $V = 0$ and pH $= 0$. *R*, *T*, *F*, and N_v are the gas constant, temperature, Faraday's constant, and Avogadro's number, respectively.

The apparent mean breakdown potential, E_b (V_c), for HDSS 2707 in NaBr solution is found to decrease linearly with the logarithm of bromide activity, as shown in Fig. 5, which is in accorded with the PDM prediction in Eq. (10). According to these data, E_b can be described as a function of a_{Br^-} ($v = 1.667$ mV/s):

$$E_b = 0.63126 - 0.30597 log[a_{Br^-}] \tag{14}$$

Consequently, the value of α (the polarizability of bl/solution interface) is determined as $α = 0.22$, which is similar to the value for AISI Type 403 SS in borate buffer solutions ($α = 0.23$) [32], and Type 436 FSS in NaCl solutions ($α = 0.29$) [33], indicating that α depends both on the material and the solution.

As described in Eq. (10), the breakdown potential of the passive film can be reformulated as [22,25]:

$$E_b = V_0 - \frac{\beta}{\alpha}pH - \frac{2.303RT}{\alpha F}log[\alpha_{Br^-}] \tag{15}$$

The mean breakdown potential, E_b, for HDSS 2707 in 1 M NaBr solution is found to increase linearly with the increasing of pH, as shown in Fig. 6. This linear relationship between E_b and pH is expressed as:

$$E_b = 0.32897 + 0.04791pH \tag{16}$$

Based on the Eq. (15), β is determined to be −0.0105 by the slope, which is consistent with the other results of the alloys, suggesting that β is more independent than α [24,30,32,37]. According to Eqs. (14) to

(16), the calculated V_0 value is 0.268 V_{SCE} and 0.281 V_{SCE}, respectively. It is worth noting that the V_0 obtained by these two methods is very similar, implying the rationality of PDM in accounting for passivity breakdown of HDSS 2707.

Fig. 7 shows the linear relationship between the breakdown potential E_b (or V_c) of the passive film and potential scan rate (*v*). The PDM also predicts the slope of the plot of the V_c vs the square root of potential scan rate ($v^{1/2}$), which is defined as [38]:

$$V_c(v) = (\frac{2\xi RT}{J_m \chi \alpha F})^{1/2}v^{1/2} + V_c(v = 0) \tag{17}$$

where V_c ($v = 0$) is regarded as the breakdown potential of passive film when the scan rate is zero. As V_c is determined potentiodynamically at scan rates that vary from study-to-study, an important use of Eq. (17) is to correct the apparent value of V_c for scan rate dependence so as to yield the steady-state value, such as obtained in a long-term immersion experiment, V_c ($v = 0$) [24,30]. ζ and J_m are the critical areal cation vacancy concentration and the rate of annihilation of cation vacancies at the bl/metal interface, respectively. Employing the value of α determined above, the ration of ζ/J_m can be calculated from the slope. As a function of $v^{1/2}$, the E_b/V_c follows:

$$E_b = 0.60435 + 1.08331v^{1/2} \tag{18}$$

For different bromide ion concentrations at 70 °C, the relationships between E_b /V_c of HDSS 2707 and the square root of the potential scan rate ($v^{1/2}$) are shown in Fig. 8. It is observed that the slope of the linear function is independent of bromide ion concentrations, as required by Eq. (17). Combining Eq. (17) and Fig. 8, it is noted that the breakdown potential at a scan rate of zero, i.e., V_c ($v = 0$) of HDSS 2707 in 1 M, 2 M and 3 M NaBr solutions at 70 °C are 0.604 V_{SCE}, 0.546 V_{SCE} and 0.466 V_{SCE}, respectively. Obviously, the critical breakdown potential, V_c
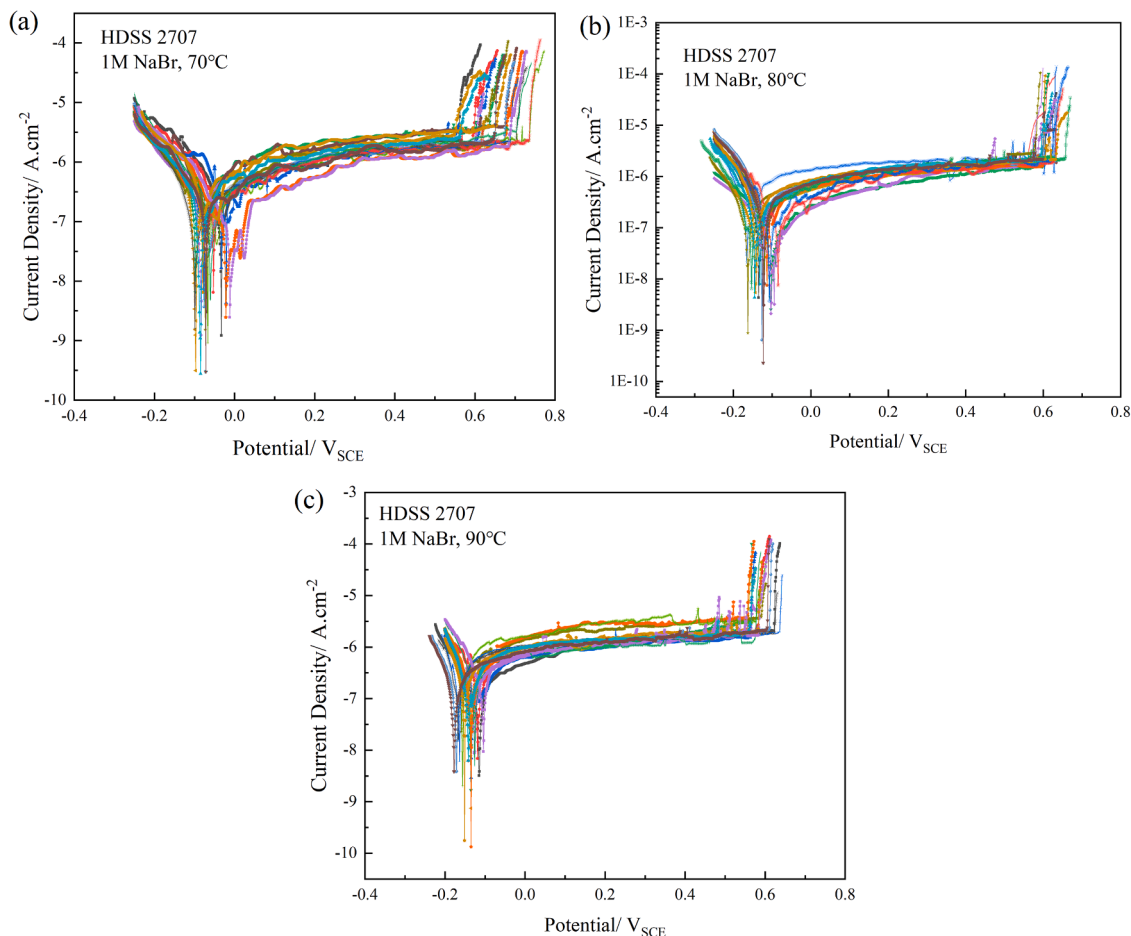
Fig. 14. Replication of potentiodynamic polarization curves for HDSS 2707 in 1 M NaBr solutions at different temperatures: (a) 70 °C; (b) 80 °C; (c) 90 °C.

($v = 0$), decreases with the increasing of bromide ion concentrations.

The maximum passive current density (I_{ss}) below the breakdown potential is used to estimate the J_m of cation vacancies at the metal/bl interface in terms of Eq. (19). The value of ζ can be subsequently obtained.

$$J_m = \frac{I_{ss}N_A}{\chi F} \tag{19}$$

where $N_A = 6.023 \times 10^{23}$ No./mol. $\chi = 3$, corresponding to Cr_2O_3. The maximum I_{ss} is estimated to be equal to 10 μA/cm² from Fig. 3. It should be noted that, the passive film on HDSS 2707 surface in NaBr solution is an n-type semiconductor, by observing a positive slope in Fig. 9, implying that the dominant defects are cation interstitials (most likely) and/or oxygen vacancies rather than cation vacancies [28]. Accordingly, the fraction of the current density carried by cation vacancies must be less than that indicated by the measured passive current density (I_{ss}) from Fig. 1. Therefore, at breakdown, the order of J_{ca} and J_m obeys Eq. (20). Thus, by assuming that cation interstitials are the main condensing species, J_m and J_{ca} are estimated to be less than 2.1×10^{13} cm⁻²s⁻¹, and ζ is therefore less than 2.5×10^{14} cm⁻².

$$\frac{I_{ss}N_v}{\chi F} > J_{ca} \geq J_m \tag{20}$$

The critical areal vacancy concentration ζ (cm⁻²) that leads to the passivity breakdown can be estimated from the unit cell dimension of the barrier layer and the substrate of the steel, depending on the lattice cation vacancy condensation. The unit cell of the barrier layer on HDSS 2707 (assumed to be Cr_2O_3) is rhombohedral with lattice parameters of a = 0.493 nm and c = 1.358 nm [33], and Cr is body centered cubic

(BCC) with the lattice parameters of a = 0.288 nm or face centered cubic (FCC) with the lattice parameters of a = 0.493 nm [39]. The density of Cr atoms per unit area in a monolayer of the unit cell is computed as $\sim10^{15}$ cm⁻² for the steel substrate and $\sim10^{14}$ cm⁻² for the chromic barrier layer. Thus, the condensation of the defects will occur on either the steel side or the barrier layer side. The results are in excellent agreement with the ζ value of HDSS 2707 calculated from the experimental data by employing the V_c as a function of potential scan rate (v), as proposed by PDM.

According to the basic M-S equation, the defect density within the passive film of HDSS 2707 in NaBr solution is calculated from the slope of the linear region in C^{-2} vs. V profiles. The basic M-S equation for n-type semiconductor is shown as follows:

$$C^{-2} = \frac{2}{eN_D\varepsilon\varepsilon_0}(V - V_{fb} - \frac{kT}{e}) \tag{21}$$

where C is the space charge capacitance, e is the elementary charge (1.6×10^{-19} C), ε_0 is the vacuum permittivity (8.85×10^{-14} *F/cm*), ε is the dielectric constant of the passive film (assumed as 12 for the chromic barrier layer [34,40]), V_{fb} is the flat band potential of the film, k is Boltzmann's constant (1.38×10^{-23} J/K), T is the Kelvin temperature (K), and N_D is the donor (point defect) density. On the basis of Eq. (21) and Fig. 9, the donor densities can be calculated. Accordingly, N_D, in 0.5 M, 1 M, 2 M and 3 M NaBr solutions are 4.45×10^{20} cm⁻³, 1.34×10^{21} cm⁻³, 1.73×10^{21} cm⁻³ and 3.93×10^{21} cm⁻³, respectively. The lower the slope, the higher the donor densities. The thickness of the passive film (L_{ss}) formed on stainless steel is usually of the nanometer scale (nm = 1×10^{-7} cm) [41]; thus, the estimated density of Cr atoms per unit volume for the barrier layer is around 10^{21} cm⁻³ from
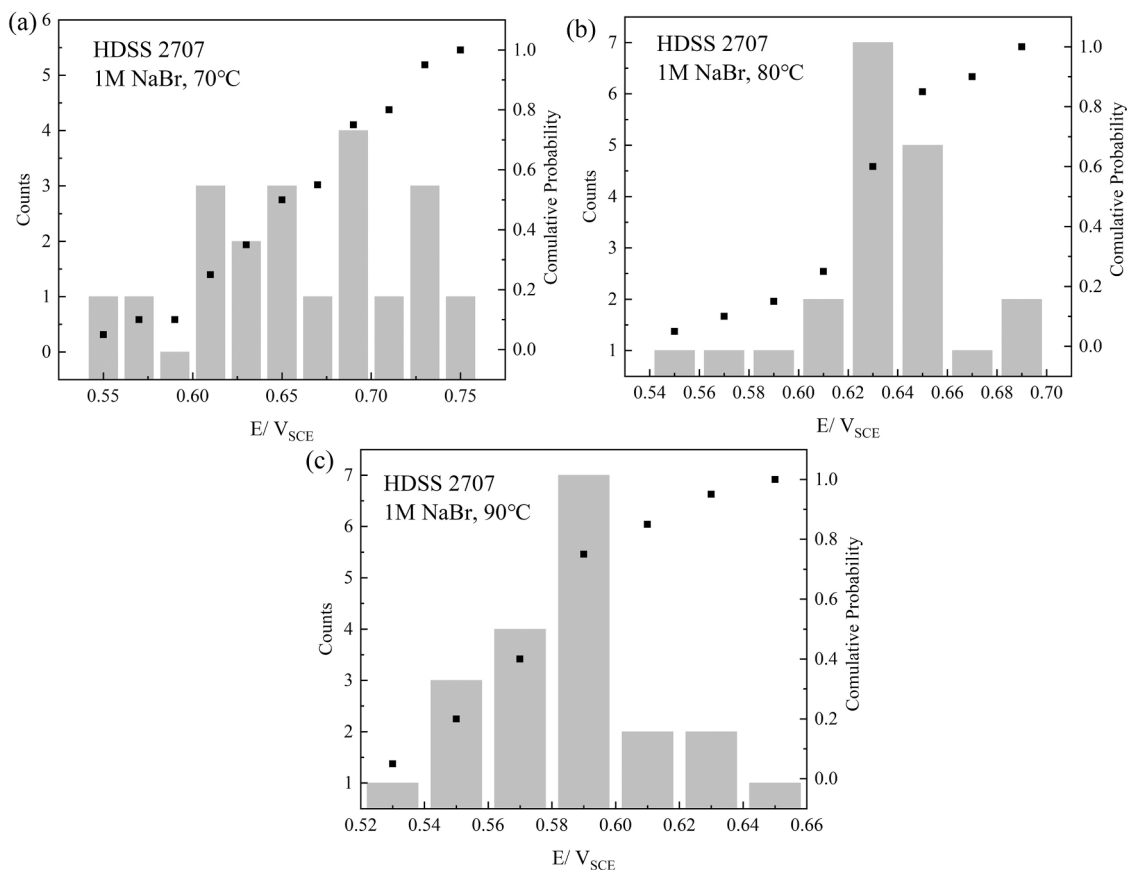
Fig. 15. Cumulative distributions of breakdown potential (V_c/E_b) in 1 M NaBr at different temperatures: (a) 70 ℃; (b) 80 ℃; (c) 90 ℃.

the unit cell dimension ($\sim 10^{14}$ cm^{-2} / L_{ss}), which is in accorded with the M-S test results and PDM analysis (ζ / L_{ss}).

3.2. The effect of temperature on pitting

Temperature is another key factor that affects the breakdown potential. The polarization curves of HDSS 2707 in 1 M NaBr solution at different temperatures are displayed in Fig. 10. It is seen that the polarization curves have a wide passivation region, from 0.1 V_{SCE} to 0.5 V_{SCE}, and the passive current density is $\sim 10^{-6}$ A/cm^2, illustrating the excellent pitting resistance of HDSS 2707. With increasing temperature, the breakdown potential (E_b) gradually decreases because the rates of point defect generation/annihilation reactions increase (Reaction R1 and R4 in Fig. 1) and the diffusivity of cation vacancies is enhanced, which enhances the accumulation of the vacancies at the bl/metal interface and thereby inducing passivity breakdown at a lower potential.

Fig. 11 shows the relationships between E_b of HDSS 2707 and the square root of the potential scan rate ($v^{1/2}$) in 1 M NaBr at different temperatures. Combining Fig. 7 and Fig. 11, we can see that the slope increases with the increasing of temperature. Based on Eq. (17), the calculated ζ are 2.5×10^{14} cm^{-2}, 2.7×10^{14} cm^{-2} and 3.3×10^{14} cm^{-2} at 70 ℃, 80 ℃ and 90 ℃, respectively, manifesting that the critical concentration of cation vacancies increases slightly while the breakdown potential decreases with the temperature. However, it must be recognized that this result is somewhat equivocal, because we do not know the fraction of the total passive current density is due to the migration of cation vacancies in contrast to that due to the migration of donor point defects (oxygen vacancies and metal interstitials). Strictly speaking, only the fraction of the observed passive current due to the migration of cation vacancies should be used in Eq. (20) in determining ζ. Unfortunately, we do not yet have a method for determining that

fraction, but the optimization of the full, seven reaction PDM on wide band EIS data holds significant promise. Nevertheless, the calculated values of ζ are consistent with the cation vacancies occupying a monolayer of cation sites ($10^{14} \sim 10^{15}$) at the m/bl interface on either the metal lattice or on the cation sublattice of the barrier layer. For a potential scan rate of zero, i.e., V_c ($v = 0$), the breakdown potentials of HDSS 2707 in 1 M NaBr solution at 70 ℃, 80 ℃ and 90 ℃ are calculated as 0.604 V_{SCE}, 0.575 V_{SCE} and 0.500 V_{SCE}, respectively. Thus, the critical breakdown potential, V_c ($v = 0$), decreases with increasing temperature, implying that during an immersion test, where the OCP gradually increases with time (as predicted theoretically by the PDM [42] confirmed by the 343 days of measured OCP values for P355 QL2 carbon steel in Ca (OH)$_2$ + NaOH solution [35]), the corrosion potential (ECP) ultimately may become greater than the critical breakdown potential, thereby ensuring spontaneous pitting [43,44] is the PDM postulates that the cation vacancies are apt to accumulate at the site of inclusions (e.g., MnS [45]), dislocations [46] and precipitates (e.g., M$_{23}$C$_6$ [47]); these being sites of high lattice disorder at their intersection with the barrier layer that are characterized by high cation vacancy diffusivity in the layer. Accordingly, these are the preferred sites for pit nucleation.

3.3. The distribution law for E_b/V_c

According to the PDM, the potential breakdown sites are assumed to distributed normally with respect to the cation vacancy diffusivity with the distribution being characterized by a mean value, $\overline{D}$, and a standard deviation, σ_D [48]. Based on this postulate, an analytical distribution function for breakdown potential, E_b/V_c, is readily derived from Eq. (22) [49].

Table 1

Parameter values used in calculating cumulative probabilities in the breakdown potential for HDSS 2707 in NaBr solutions with different bromide concentrations at different temperatures.

Parameters	Values	Units	Sources
F, Faraday's constant.	96,487	$C/$equiv	Constant
R, the gas constant.	8.314	$J/($mol K$)$	Constant
pH	8.2 ± 0.2	–	Measured
N_A, Avogadro's number.	6.023×10^{23}	No./mol	Constant
χ, the barrier layer stoichiometry (Cr_2O_3).	3	–	Assigned
$\bar{\varepsilon}$, the electric field strength within the bl.	1×10^6	$V/$cm	Assumed
α, the dependence of $\phi_{f/s}$ on the applied voltage.	0.22	–	From Fig. 5.
β, the dependence of $\phi_{f/s}$ on pH.	-0.0105	V	From Fig. 6.
Ω, molar volume of Cr_2O_3 per cation.	14.59	$cm^3/$mol	From density
$\bar{D}$, the mean diffusivity. of cation vacancy.	2×10^{-20} (343.15 K) 4×10^{-20} (353.15 K) 1×10^{-19} (363.15 K)	cm^2/s	Fitted from Fig. 17.
J_m, the rate of annihilation of cation vacancy at m/bl interface.	2.1×10^{13}	No./(cm^{2}s)	Calculate
ζ, the critical areal cation vacancy concentration.	2.5×10^{14} (343.15 K) 2.7×10^{14} (353.15 K) 3.3×10^{14} (363.15 K)	No./cm^2	From Fig. 11.
N_D, donor density.	4.45×10^{20} (0.5 M) 1.34×10^{21} (1.0 M) 1.73×10^{21} (2.0 M) 3.93×10^{21} (3.0 M)	No./cm^3	From Fig. 9.
$\gamma' = \dfrac{\chi \alpha F}{2RT}$	11.16 (343.15 K) 10.84 (353.15 K) 10.55 (363.15 K)	V^{-1}	Calculated
w, energy term.	-7.29	kJ/mol	Calculated
σ_D, the standard deviation for the cation vacancy diffusivity.	9×10^{-21} (2 M, 3 M) 1.3×10^{-20} (0.5 M, 1 M) 1.3×10^{-20} (343.15 K) 9×10^{-21} (353.15 K) 9×10^{-21} (363.15 K)	cm^2/s	Fitted from Fig. 16 and Fig. 17.

$$\frac{dN}{dV_c} = \frac{-\gamma' D}{\sqrt{2\pi} \cdot \sigma_D} exp\left[-\left(\frac{D - \bar{D}}{\sqrt{2} \cdot \sigma_D}\right)^2\right]$$

$$= \frac{-b\gamma'}{\sqrt{2\pi} \cdot \sigma_D \cdot a_{Cl-}^{\chi/2}} exp\left[\frac{-\left(e^{-\gamma' v_c} - e^{-\gamma' \bar{v}_c}\right)^2 b^2}{2 \cdot \sigma_D^2 \cdot a_{Cl-}^{\chi}}\right] exp\left(-\gamma' V_c\right) \quad (22)$$

where $\gamma' = \frac{\chi \alpha F}{2RT}$, $\frac{dN}{dV_c} = \frac{dN}{dD}/\frac{dV_c}{dD}$, $\frac{dV_c}{dD}$ is derived from Eq. (10). $\bar{V}_c$ is mean breakdown potential, which is expressed as follows:

$$\bar{V}_c = \frac{1}{\gamma'} ln\left(\frac{b}{D} \cdot a_{Br-}^{\chi/2}\right) \quad (23)$$

The cumulative probability in breakdown potential is defined as Eq. (24), where $P(V_c)$ represents the percentage of breakdown sites at V_c in all possible breakdown sites.

$$P(V_c) = 100 \times \frac{\int_{-\infty}^{V_c} \left(\frac{dN}{dV_c}\right) dV_c}{\int_{-\infty}^{+\infty} \left(\frac{dN}{dV_c}\right) dV_c} \quad (24)$$

The relationship of $P(V_c)$ versus V_c is given by Eqs. (22) to (24). Combined with experimental results, this provides a sensitive prediction of the fundamental nature of, and the theory for, the distribution of breakdown sites on the metal surface.

Fig. 12 and Fig. 13 show the typical replicate potentiodynamic polarization curves for HDSS 2707 in different bromide ion concentrations at 70 ℃, and the statistics of the V_c along with the cumulative distributions, respectively. It is evident that the distribution range of the breakdown potential is less than 200 mV$_{SCE}$ (Fig. 13), ultimately defining the fundamental limit on the reproducibility of V_c. Literature reviews indicate that the distribution range of breakdown potential values from replicated measurements increases with (a) a decrease in the exposed area, (b) an increase in the alloying content or a decrease in the susceptible microstructural surface features (e.g., roughness), and (c) a decrease in the environmental aggressiveness [50–52]. In this paper, the distribution range of breakdown potential of HDSS 2707 is larger than for any other metals reported to date [24,31,33,39], which is attributed to the high alloying content of HDSS 2707.

Fig. 14 and Fig. 15 show typical replicate potentiodynamic polarization curves for HDSS 2707 in 1 M NaBr solution at different temperatures, and the statistics of the V_c and the cumulative distributions, respectively. It is seen that the distribution in the breakdown potential (V_c) decreases with the increasing of temperature, i.e., $\Delta V_c = 200$ mV$_{SCE}$ at 70 ℃, $\Delta V_c = 140$ mV$_{SCE}$ at 80 ℃, and $\Delta V_c = 120$ mV$_{SCE}$ at 90 ℃ because of an increased aggressiveness of corrosive environment.

Based on the above analysis, the required pitting parameters of HDSS 2707 for the PDM analysis are obtained, and are listed in Table 1. These parameters for HDSS 2707 are obtained in a single [Br⁻] at each temperature. Combined with Eqs. (22)–(24), the statistical distribution in the breakdown potential for HDSS 2707 in different NaBr concentrations at different temperatures can be calculated, as shown in Fig. 16 and Fig. 17. It is clear that the calculated values are consistent with the experimental measurements, implying the rationality of the PDM for predicting pitting.

The calculated distributions in terms of the PDM use $\sigma_D = 0.65D$ in 0.5 M and 1 M NaBr solutions, and use $\sigma_D = 0.45D$ in 2 M and 3 M NaBr solutions of HDSS 2707 at 70 ℃, and hence in good agreement with the experimental measurements (Fig. 16). Typically, these experiments were repeated 20 times, in order to obtain the statistically valid distributions. A greater value of σ_D dictates that the population of breakdown sites is characterized by a wider distribution [39]. Therefore, increasing Br⁻ concentration lead to a narrowing of the distribution in the breakdown potential, which is in satisfactory agreement with Fig. 13. Similarly, the calculated distributions in terms of the PDM use $\sigma_D = 0.65D$ at 70 ℃, and use $\sigma_D = 0.45D$ at 80 ℃ and 90 ℃ of HDSS 2707 in 1 M NaBr solution for a better fit. Thus, increasing the temperature tends to decrease the standard deviation, σ_D, and to increase the mean defect diffusivity (Table 1), $\bar{D}$, at the breakdown sites, rendering the pitting probability distribution more compact. Based on previous research, we find that by lowering the number of potential breakdown sites per unit area of the surface, the parameter that would appear to be most readily manipulated to impact the susceptibility of a passive film to chemically induced breakdown is the cation vacancy diffusivity [29,30,32,33,39]. Hence, a decrease in cation vacancy diffusivity ($10^{-20} \sim 10^{-19}$ for HDSS 2707) leads to an increase in breakdown potential because a higher voltage is required to produce the same flux of cation vacancies via the barrier layer to achieve the breakdown condition ($J_{ca} \geq J_m$).
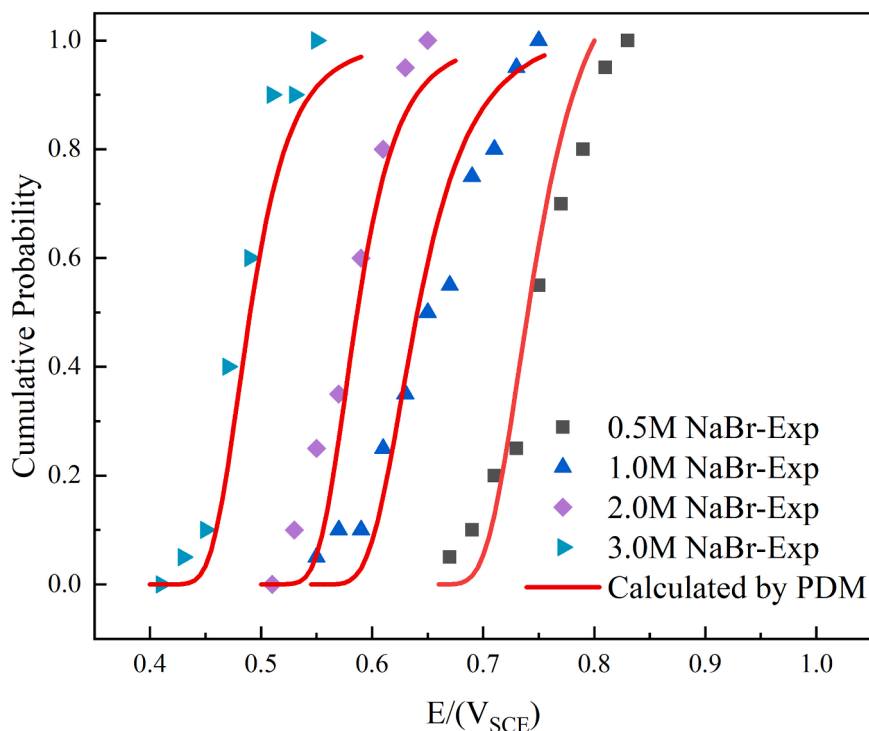
Fig. 16. Calculated cumulative probabilities in the breakdown potential for HDSS 2707 for different concentrations of NaBr solution (pH = 8.2 ± 0.2) at 70 ℃, compared with experimentally-determined distributions. The solid lines are the calculated distributions with $\sigma_D = 0.45D$ in 2 M and 3 M NaBr solutions, while $\sigma_D = 0.65D$ in 0.5 M and 1 M NaBr solutions.
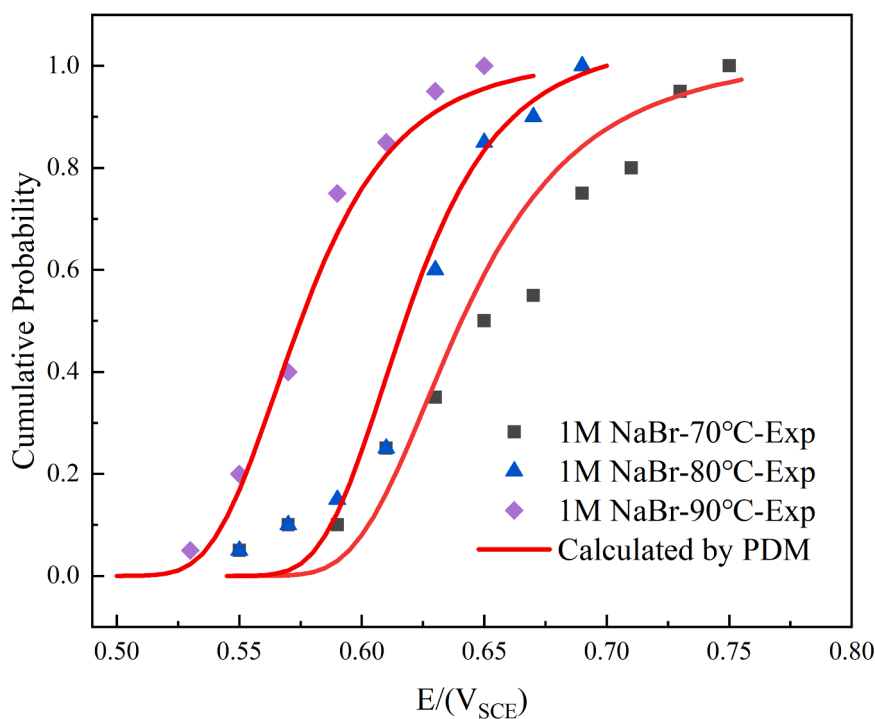

Fig. 17. Calculated cumulative probabilities in the breakdown potential for HDSS 2707 at different temperatures in 1 M NaBr solution (pH = 8.1 ± 0.2), compared with experimentally-determined distributions. The solid lines are the calculated distributions with $\sigma_D = 0.45D$ at 80 ℃ and 90 ℃, while $\sigma_D = 0.65D$ at 70 ℃.

4. Conclusions

In this work, the relationships between the breakdown potential, E_b (V_c), of passive HDSS 2707 and temperature, bromide concentration, pH, and potential scan rate were studied. The results show that the PDM

convincingly describes the pitting behavior of duplex stainless steel. The pitting parameters of HDSS 2707 are calculated, and the experimentally-determined distributions of E_b of HDSS 2707 in NaBr solutions are in line with the PDM predictions. The main conclusions are summarized as follows:

1. The polarizability of the barrier layer/solution interface (α) is 0.22 and β is -0.0105 V for HDSS 2707 in NaBr solution. The annihilation rate of cation vacancies at the metal/bl interface of HDSS 2707 is $\sim 2.1 \times 10^{13}$ cm^{-2}s^{-1}.

2. The critical areal cation vacancy concentration (ζ) for passivity breakdown, analyzed by PDM, is calculated to be about $\sim 10^{14}$ cm^{-2}, and tends to increase with temperature, which is in excellent agreement with that estimated from steel crystal structure and M-S measurements, although this latter result is equivocal because the fraction of the observed passive current density due to the migration of cation vacancies is currently unknown.

3. Statistical analysis of the experimentally determined breakdown potential (E_b) of HDSS 2707 shows that E_b follows a near-normal distribution as predicted by the PDM.

4. Both increasing of bromide ion concentrations and the temperatures tend to shift the distributions of breakdown potential (E_b) to more negative potentials, and lead to a narrow distribution in E_b, thereby having a decreased in standard deviation, σ_D, for an optimal fit of the theoretical distribution function to the experimental data.

5. Correlation between experimental data on the breakdown potential (E_b) as functions of bromide ion concentration, temperature, pH, and potential scan rate demonstrates the validity of PDM in analyzing the breakdown behaviors of HDSS 2707.

CRediT authorship contribution statement

Li Sun: Conceptualization, Methodology, Experiment, Data curation, Writing. **Tianyu Zhao:** Data curation, Editing. **Jie Qiu:** Methodology, Editing. **Yangting Sun:** Conceptualization, Supervision, Project administration, Editing. **Kuijiao Li:** Experiment. **Haibing Zheng:** Editing. **Yiming Jiang:** Data curation, Editing. **Yanhui Li:** Methodology. **Jin Li:** Data curation. **Weihua Li:** Editing. **Digby D. Macdonald:** Methodology, Data curation, Editing, Supervision.

Declaration of Competing Interest

The authors declare that they have no known competing financial interests or personal relationships that could have appeared to influence the work reported in this paper.

Acknowledgements

References

[1] H. Li, E. Zhou, D. Zhang, D. Xu, J. Xia, C. Yang, H. Feng, Z. Jiang, X. Li, T. Gu, Microbiologically influenced corrosion of 2707 hyper-duplex stainless steel by marine Pseudomonas aeruginosa biofilm, Sci. Rep. 6 (2016) 1–12.

[2] K. Göransson, M.-L. Nyman, M. Holmquist, E. Gomes, Sandvik SAF 2707 HD®(UNS S32707): a hyper-duplex stainless steel for severe chloride containing environments, Metall. Res. Technol. 104 (2007) 411–417.

[3] L. Sun, Y. Sun, Y. Liu, N. Dai, J. Li, Y. Jiang, Effect of annealing temperature on pitting behavior and microstructure evolution of hyper-duplex stainless steel 2707, Mater. Corros. 70 (2019) 1682–1692.

[4] K. Deen, M. Virk, C. Haque, R. Ahmad, I. Khan, Failure investigation of heat exchanger plates due to pitting corrosion, Eng. Fail. Anal. 17 (2010) 886–893.

[5] W. Wu, G. Cheng, H. Hu, Q. Zhou, Risk analysis of corrosion failures of equipment in refining and petrochemical plants based on fuzzy set theory, Eng. Fail. Anal. 32 (2013) 23–34.

[6] M. Meriem-Benziane, B. Bou-Saïd, B.G.N. Muthanna, I. Boudissa, Numerical study of elbow corrosion in the presence of sodium chloride, calcium chloride, naphthenic acids, and sulfur in crude oil, J. Petrol. Sci. Eng. 198 (2021), 108124.

[7] J. Galvele, R. Torresi, R. Carranza, Passivity breakdown, its relation to pitting and stress-corrosion-cracking processes, Corros. Sci. 31 (1990) 563–571.

[8] S.M. Kim, J.S. Kim, K.T. Kim, K.-T. Park, Y.S. Park, C.S. Lee, Effect of Si and Ce addition on the microstructure and pitting corrosion resistance of hyper-duplex stainless steels, Corrosion 71 (2015) 470–482.

[9] S.-H. Jeon, D.H. Hur, H.-J. Kim, Y.-S. Park, Effect of Ce addition on the precipitation of deleterious phases and the associated intergranular corrosion resistance of 27Cr–7Ni hyper duplex stainless steels, Corros. Sci. 90 (2015) 313–322.

[10] S.-H. Jeon, S.-T. Kim, I.-S. Lee, J.-S. Kim, K.-T. Kim, Y.-S. Park, Effects of Cu on the precipitation of intermetallic compounds and the intergranular corrosion of hyper duplex stainless steels, Corros. Sci. 66 (2013) 217–224.

[11] S.-H. Jeon, S.-T. Kim, I.-S. Lee, J.-S. Kim, K.-T. Kim, Y.-S. Park, Effects of W substitution on the precipitation of secondary phases and the associated pitting corrosion in hyper duplex stainless steels, J. Alloy. Compd. 544 (2012) 166–172.

[12] S.-T. Kim, S.-H. Jang, I.-S. Lee, Y.-S. Park, Effects of solution heat-treatment and nitrogen in shielding gas on the resistance to pitting corrosion of hyper duplex stainless steel welds, Corros. Sci. 53 (2011) 1939–1947.

[13] L. Sun, Y. Sun, C. Lv, Y. Liu, N. Dai, Y. Jiang, J. Li, D.D. Macdonald, Studies on the degree of sensitization of hyper-duplex stainless steel 2707 at 900°C using a modified DL-EPR test, Corros. Sci. (2021), 109432.

[14] J. Wang, W.-l Chen, H.-j Meng, Y.-s Cui, C.-l Zhang, Influence of sigma phase on corrosion and mechanical properties of 2707 hyper-duplex stainless steel aged for short periods, J. Iron Steel Res. Int. 26 (2019) 452–461.

[15] B. Zhang, Z. Jiang, H. Li, S. Zhang, H. Feng, H. Li, Precipitation behavior and phase transformation of hyper duplex stainless steel UNS S32707 at nose temperature, Mater. Charact. 129 (2017) 31–39.

[16] C. Chao, L. Lin, D. Macdonald, A point defect model for anodic passive films: I. Film growth kinetics, J. Electrochem. Soc. 128 (1981) 1187.

[17] L. Lin, C. Chao, D. Macdonald, A point defect model for anodic passive films: II, Chem. Breakdown Pit. Initiat. J. Electrochem. Soc. 128 (1981) 1194.

[18] C. Chao, L. Lin, D. Macdonald, A point defect model for anodic passive films: III, Impedance Response J. Electrochem. Soc. 129 (1982) 1874.

[19] D.D. Macdonald, S.R. Biaggio, H. Song, Steady-state passive films: Interfacial kinetic effects and diagnostic criteria, J. Electrochem. Soc. 139 (1992) 170.

[20] D. Ellerbrock, D.D. Macdonald, Passivity of titanium, part 1: film growth model diagnostics, J. Solid State Electrochem 18 (2014) 1485–1493.

[21] D.J. Ellerbrock, D.D. Macdonald, Passivity breakdown on solid versus liquid gallium, J. Electrochem. Soc. 141 (1994) 2645.

[22] D.D. Macdonald, The point defect model for the passive state, J. Electrochem. Soc. 139 (1992) 3434.

[23] S. Yang, D.D. Macdonald, Theoretical and experimental studies of the pitting of type 316L stainless steel in borate buffer solution containing nitrate ion, Electrochim. Acta 52 (2007) 1871–1879.

[24] F. Mao, C. Dong, S. Sharifi-Asl, P. Lu, D.D. Macdonald, Passivity breakdown on copper: influence of chloride ion, Electrochim. Acta 144 (2014) 391–399.

[25] D.D. Macdonald, PassivityÐthe key to our metals-based civilization, Pure Appl. Chem. 71 (1999) 951–978.

[26] D.D. Macdonald, Some personal adventures in passivity—a review of the point defect model for film growth, Russ. J. Electrochem. 48 (2012) 235–258.

[27] D.D. Macdonald, M. Urquidi-Macdonald, Theory of steady-state passive films, J. Electrochem. Soc. 137 (1990) 2395.

[28] J. Qiu, D.D. Macdonald, Y. Xu, L. Sun, General corrosion of carbon steel in a synthetic concrete pore solution, Mater. Corros. 72 (2021) 107–119.

[29] E. Ghanbari, A. Saatchi, X. Lei, D. Kovalov, D.D. Macdonald, Passivity breakdown and pitting corrosion of Al-Li aerospace alloys, in: Proceedings of the 2017 DoD Allied Nations Technical Corrosion Conference, Birmingham, AL, USA, 2017, pp. 7–10.

[30] S. Zhou, Q. Yan, C. Tang, F. Mao, J. Pu, D.D. Macdonald, Effect of the chloride on passivity breakdown of Al-Zn-Mg alloy, Corros. Sci. 163 (2020), 108254.

[31] J. Zhong, M. Yu, S. Li, D.D. Macdonald, B. Xiao, J. Liu, Theoretical and experimental studies of passivity breakdown of Aermet 100 ultra-high strength steel in chloride ion medium, Mater. Corros. 70 (2019) 2020–2032.

[32] Y. Zhang, D.D. Macdonald, M. Urquidi-Macdonald, G.R. Engelhardt, R.B. Dooley, Passivity breakdown on AISI Type 403 stainless steel in chloride-containing borate buffer solution, Corros. Sci. 48 (2006) 3812–3823.

[33] J. Wang, S. Qian, Y. Li, D.D. Macdonald, Y. Jiang, J. Li, Passivity breakdown on 436 ferritic stainless steel in solutions containing chloride, J. Mater. Sci. Technol. 35 (2019) 637–643.

[34] J. Yao, D.D. Macdonald, C. Dong, Passive film on 2205 duplex stainless steel studied by photo-electrochemistry and ARXPS methods, Corros. Sci. 146 (2019) 221–232.

[35] D.D. Macdonald, J. Qiu, S. Sharifi-Asl, J. Yang, G.R. Engelhardt, Y. Xu, E. Ghanbari, A. Xu, A. Saatchi, D. Kovalov, Pitting of carbon steel in the synthetic concrete pore solution, Mater. Corros. (2020).

[36] P. Lu, G.R. Engelhardt, B. Kursten, D.D. Macdonald, The kinetics of nucleation of metastable pits on metal surfaces: the Point Defect Model and its optimization on data obtained on stainless steel, carbon steel, iron, aluminum and Alloy-22, J. Electrochem. Soc. 163 (2016) C156.

[37] L. Bertolini, F. Bolzoni, T. Pastore, P. Pedeferri, Behaviour of stainless steel in simulated concrete pore solution, Br. Corros. J. 31 (1996) 218–222.

[38] T. Haruna, D.D. Macdonald, Theoretical prediction of the scan rate dependencies of the pitting potential and the probability distribution in the induction time, J. Electrochem. Soc. 144 (1997) 1574.

[39] J. Zhong, F. Mao, E. Ghanbari, D.D. Macdonald, Passivity breakdown on 300 M and S280 ultra-high strength steels in borate buffer solutions containing chloride ion, Electrochim. Acta 251 (2017) 324–335.

[40] C. V. L'hostis, D. Dagbert, Féron, Electrochemical behavior of metallic materials used in seawater—interactions between glucose oxidase and passive layers, Electrochim. Acta 48 (2003) 1451–1458.

[41] M. Långberg, F. Zhang, E. Grånäs, C. Örnek, J. Cheng, M. Liu, C. Wiemann, A. Gloskovskii, T. Keller, C. Schlueter, Lateral variation of the native passive film on super duplex stainless steel resolved by synchrotron hard X-ray photoelectron emission microscopy, Corros. Sci. 174 (2020), 108841.

[42] D.D. Macdonald, Theoretical investigation of the evolution of the passive state on Alloy 22 in acidified, saturated brine under open circuit conditions, Electrochim. Acta 56 (2011) 7411–7420.

[43] D.D. Macdonald, J. Qiu, Y. Zhu, J. Yang, G.R. Engelhardt, A. Sagüés, Corrosion of rebar in concrete. Part I: calculation of the corrosion potential in the passive state, Corros. Sci. 177 (2020), 109018.

[44] D.D. Macdonald, Y. Zhu, J. Yang, J. Qiu, G.R. Engelhardt, A. Sagüés, L. Sun, Z. Xiong, Corrosion of rebar in concrete. Part IV. On the theoretical basis of the chloride threshold, Corros. Sci. (2021), 109460.

[45] D.D. Macdonald, D.F. Heaney, Effect of variable intensity ultraviolet radiation on passivity breakdown of AISI Type 304 stainless steel, Corros. Sci. 42 (2000) 1779–1799.

[46] L. Peguet, B. Malki, B. Baroux, Influence of cold working on the pitting corrosion resistance of stainless steels, Corros. Sci. 49 (2007) 1933–1948.

[47] Z. Zhang, H. Zhao, H. Zhang, Z. Yu, J. Hu, L. He, J. Li, Effect of isothermal aging on the pitting corrosion resistance of UNS S82441 duplex stainless steel based on electrochemical detection, Corros. Sci. 93 (2015) 120–125.

[48] M. Urquidi-Macdonald, D.D. Macdonald, Theoretical distribution functions for the breakdown of passive films, J. Electrochem. Soc. 134 (1987) 41.

[49] D.D. Macdonald, M. Urquidi-Macdonald, Distribution functions for the breakdown of passive films, Electrochim. Acta 31 (1986) 1079–1086.

[50] G. Salvago, G. Fumagalli, Application of breakdown potential distribution in corrosion comparisons of stainless steels, Corrosion 52 (1996) 760–767.

[51] G. Salvago, G. Fumagalli, The distribution of the breakdown potential of stainless steels: effects of test repetition, specimen exposure surfaces and threshold current, Corros. Sci. 37 (1995) 1303–1312.

[52] T. Li, J. Wu, G. Frankel, Localized corrosion: Passive film breakdown vs. Pit growth stability, Part VI: Pit dissolution kinetics of different alloys and a model for pitting and repassivation potentials, Corros. Sci. 182 (2021), 109277.